



Modulating d-orbital occupancy via a coupled interfacial-local electric field for electrocatalytic N₂ fixation

Xiaoxuan Wang^a, Jingxian Li^a, Yingjie Ji^a, Shuyuan Li^a, Shiyu Wang^a, Yanfei Sun^a,
Xueying Gao^a, Zheng Tang^a, Huiying Zhang^a, Feike Zhang^a, Jiangzhou Xie^{b,*}, Zhiyu Yang^{a,*},
Yi-Ming Yan^{a,*}

^a State Key Laboratory of Organic-Inorganic Composites, Beijing Advanced Innovation Center for Soft Matter Science and Engineering, Beijing University of Chemical Technology, Beijing 100029, People's Republic of China

^b School of Mechanical and Manufacturing Engineering, University of New South Wales, Sydney, New South Wales 2052, Australia

ARTICLE INFO

Keywords:

Nitrogen reduction reaction
 d_z^2 occupancy
Interfacial-local electric field
Electron transfer

ABSTRACT

The electrocatalytic nitrogen reduction reaction (ENRR) offers a sustainable and cost-effective strategy for ammonia (NH₃) synthesis. However, the broad applicability of ENRR is currently limited by challenges in the adsorption and activation of N₂ at the catalyst interface. Addressing these issues, we have developed an innovative approach that constructs an interfacial electric field, coupled with an atomically local electric field induced by W-N bonds. This coupled interfacial-local electric field effectively elevates the d_z^2 occupancy of W active sites, thereby significantly enhancing the adsorption and activation of N₂. This work provides profound insights into the relationship between the interfacial-local electric field and the efficient execution of ENRR, paving the way for future explorations and potential breakthroughs within catalytic field.

1. Introduction

Ammonia (NH₃), a bedrock material in the development and production of various commodities such as fertilizers, pharmaceuticals, explosives, pigments, synthetic resins, and plastics, fundamentally underpins numerous aspects of human and economic progress [1,2]. Nonetheless, the traditional method of NH₃ production—the Haber-Bosch process—is notorious for its energy intensity, demanding temperatures of 400–500 °C and pressures of 20–40 MPa [3,4]. Moreover, the reliance of this process on fossil fuels, and its concomitant release of copious CO₂ emissions, underscore the need for alternative methods [5–10]. The electrochemical nitrogen reduction reaction (ENRR) represents a promising route to this end, offering a carbon-neutral pathway for NH₃ production. ENRR [11–13], a promising alternative to the Haber-Bosch process, operates under ambient conditions, yielding benefits in reduced energy consumption and CO₂ emissions mitigation [14–17]. However, ENRR technology presently faces critical challenges, such as substandard activity and low selectivity, primarily attributable to insufficient N₂ adsorption and activation [18–21].

The d_z^2 orbital of transition metals, renowned for its distinctive shape

and spatial distribution, has emerged as an essential player in reactant adsorption, thereby enhancing electrochemical reaction kinetics. A striking example of this involves the regulation of d_z^2 orbital occupancy in Co and Fe, adjusting the adsorption strength of O₂ and CO₂ and subsequently increasing the electrochemical reaction rate [22–24]. Consequently, the development of effective methods for regulating d_z^2 orbital occupancy is pivotal for enhancing ENRR performance. The electric field, a potent tool for regulating orbital occupancy in transition metals, is broadly categorized into local and interfacial electric fields. A local electric field typically arises from specially designed high curvature structures [25–28] and heteroatom doping [29,30]. Conversely, an interfacial electric field is constructed between suitable heterostructure materials [31–37]. Both types of electric fields are recognized for their ability to regulate the orbital occupancy of transition metals, augmenting the adsorption of reactants and intermediates. For instance, Sargent et al. firstly constructed a local electric field at an Au electrocatalyst to bolster CO₂ molecule polarization for electrocatalytic carbon dioxide reduction [27]. Similarly, Liu et al. introduced Sn atoms to an Ag catalyst, resulting in potent and localized electric field to enhance the adsorption of *COOH [30]. In addition, Yan et al. strategically designed WS₂-WO₃ heterostructure induced a robust interfacial electric field to

* Corresponding authors.

E-mail addresses: jiangzhou.xie@unsw.edu.au (J. Xie), yangzhiyu@mail.buct.edu.cn (Z. Yang), yanym22@mail.buct.edu.cn (Y.-M. Yan).

<https://doi.org/10.1016/j.apcatb.2024.123700>

Received 15 November 2023; Received in revised form 29 December 2023; Accepted 3 January 2024

Available online 4 January 2024

0926-3373/© 2024 Elsevier B.V. All rights reserved.

elevate the d-band center of W, resulting a substantial acceleration of ENRR kinetics [31]. Despite these advancements, there remains a significant gap in the concurrent implementation of interfacial and local (termed as interfacial-local) electric fields on the electrocatalyst surface to regulate d_z^2 orbital occupancy, offering the potential for further improved ENRR kinetics.

In this study, we successfully tailored the d_z^2 occupancy of W active sites by establishing a potent interfacial-local electric field in a $\text{WO}_3\text{-C}_3\text{N}_4$ heterostructure. Consequently, the engineered $\text{WO}_3\text{-C}_3\text{N}_4$ catalyst delivered a significantly improved NH_3 yield of $54.87 \mu\text{g h}^{-1} \text{mg}_{\text{cat}}^{-1}$ at -0.3 V versus RHE, a value markedly superior to that of the WO_3 catalyst. DFT calculations were performed to illuminate the formation mechanisms of the interfacial-local electric field and to predict its impact on d_z^2 occupancy at W active sites. Furthermore, the zeta potential and kelvin probe force microscopy (KPFM) results provided direct evidence for the presence of a robust interfacial-local electric field in the $\text{WO}_3\text{-C}_3\text{N}_4$ heterostructure. In addition, *in situ* experiments and supplementary calculations demonstrated that elevating d_z^2 occupancy of W active sites can effectively promote the N_2 adsorption and activation. These findings offer a comprehensive understanding of the influence exerted by the interfacial-local electric field on the performance of ENRR catalysts.

2. Experimental section

2.1. Synthesis of electrocatalysts

In a standard procedure, a quantity of 5.0 g of DICY was deposited in a lidded crucible and heated to a temperature of 600°C for 3 h in air atmosphere to prepare C_3N_4 . Subsequently, a blend of 150 mL of distilled water and 0.3 g of the freshly prepared C_3N_4 was subjected to sonication for a period of 30 min. Thereafter, 4 g $\text{Na}_2\text{WO}_4 \cdot 2 \text{H}_2\text{O}$ and 2 g citric acid were added to this mixture, which was then subjected to vigorous stirring for 1 h. Once the solid substances had completely dissolved, 3 mL of HCl were incorporated into the mixture, which was then positioned on a hot plate that maintained continuous stirring, and heated at a temperature of 35°C for 12 h. The resulting precipitate was subsequently centrifuged and air-dried at a temperature of 70°C . The dried materials was calcined at a temperature of 300°C to acquire the final $\text{WO}_3\text{-C}_3\text{N}_4$ product. As a control measure, a sample of WO_3 powder was also prepared utilizing the same procedure as that of the $\text{WO}_3\text{-C}_3\text{N}_4$ without the addition of C_3N_4 .

2.2. Characterizations

To observe the morphology of the catalysts, scanning electron microscopy (SEM, FEI Quanta 200), transmission electron microscopy (TEM, FEI Tecnai G2 20), and high-resolution TEM (HRTEM, JEM-2100 F, 200 kV) were employed. We procured high-angle annular dark-field scanning transmission electron microscopy (HAADF-STEM) images using a JEOL JEM-ARM200F TEM/STEM instrument. The X-ray diffraction (XRD, Rigaku D/max 2500) was carried out to analyze the crystalline structures using with $\text{Cu K}\alpha$ radiation ($\lambda = 0.15405 \text{ nm}$). We implemented ultraviolet photoelectron spectroscopy (UPS) measurements using a Thermo Scientific ESCALab 250Xi apparatus. The surface chemical status and composition were analyzed by X-ray photoelectron spectroscopy (XPS, Thermo Fisher Scientific). The surface potential of the catalysts was examined by Kelvin probe force microscopy (KPFM, Oxford MFP-3D, UK). For *in situ* Raman tests using an excitation wavelength of 532 nm, the electrochemical operando flow cell (EC-RAIR-H) was provided by Tianjin Gauss Union technology Co. Ltd. A SOPTOP LMplan objective (50X) was used for signal collection and the collection time was 30 s

2.3. Electrochemical measurements

Electrochemical experiments were conducted in a conventional H-

type cell, utilizing the CHI 760e electrochemical workstation. The working electrode was the prepared $\text{WO}_3\text{-C}_3\text{N}_4\text{/CP}$ electrode, while the counter electrode was a platinum gauze electrode, and the reference electrode was an Ag/AgCl electrode. In this study, the potentials were recalibrated to RHE using the subsequent formula. In this study, the potentials were recalibrated to RHE by the subsequent equation: $E \text{ (vs RHE)} = E \text{ (vs Ag/AgCl)} + 0.197 + 0.0591 \times \text{pH}$. Before conducting the NRR measurements, the 0.1 M Li_2SO_4 electrolyte was continuously infused with N_2 for a duration of 30 min.

2.4. Quantification of NH_3

The produced ammonia was evaluated using the indophenol blue method. Specifically, 2 mL sample of the post-tested electrolyte was extracted from the cathodic chamber and combined with 2 mL of a 1.0 M NaOH solution, containing $\text{C}_7\text{H}_6\text{O}_3$ and $\text{C}_6\text{H}_5\text{Na}_3\text{O}_7 \cdot 2 \text{H}_2\text{O}$ at a concentration of 5 wt%. Sequentially, we introduced 1 mL of a 0.05 M NaClO solution and 0.2 mL of a 1 wt% $\text{Na}_2[\text{Fe}(\text{NO})(\text{CN})_5] \cdot 2 \text{H}_2\text{O}$ aqueous solution. The blend was left to settle at room temperature for a duration of 2 h, after which the UV-vis absorption spectrum was recorded. Calibration of the concentration-absorbance relationship was done using standard NH_4Cl solutions with concentrations varying from 0.1 to $1.2 \mu\text{g mL}^{-1}$. These were prepared by diluting a $100 \mu\text{g mL}^{-1}$ NH_4Cl solution with 0.1 M Li_2SO_4 . The quantity of indophenol blue was ascertained by measuring the absorbance at a 655 nm wavelength. An observed linear relation between the absorbance value and NH_4Cl concentration yielded a fitting curve of $y = 0.2747x + 0.0334$ ($R^2 = 0.9991$), derived from three separate calibration procedures.

2.5. Calculations of yield and Faradaic efficiency

The rate of NH_3 yield was obtained as follows:

$$\text{Yield rate} = \frac{C_{\text{NH}_3} \times V}{t \times m_{\text{cat}}}$$

The FE was obtained as follows:

$$\text{FE} = \frac{3 \times F \times C_{\text{NH}_3} \times V}{17 \times Q}$$

where C_{NH_3} ($\mu\text{g mL}^{-1}$) represents the concentration of NH_3 ; F is Faraday constant ($96,500 \text{ C mol}^{-1}$); V (mL) signifies the electrolyte volume (30 mL); t (s) is the electrolysis time; m_{cat} (mg) represents the catalyst mass; Q (C) is the quantity of applied electricity.

2.6. Computational details

We implemented density functional theory (DFT) calculations utilizing the Vienna ab initio simulation package (VASP). The exchange-correlation interactions were addressed using the Perdew-Burke-Ernzerhof (PBE) functional. we utilized the DFT-D2 method to account for the van der Waals (vdW) interaction. Structural optimization involved sampling the Brillouin zone with $4 \times 3 \times 1$ k-points for a plane-wave basis. The cutoff for kinetic energy was established at 500 eV, with the SCF convergence criterion at 10^{-5} eV . We allowed all atoms to relax until the residual forces reduced to less than 0.02 eV/\AA . The vacuum space is 20 \AA along the z-direction. The change of Gibbs free energy (ΔG) of each step is calculated as follows:

$$\Delta G = \Delta E + \Delta E_{\text{ZPE}} - T\Delta S$$

3. Results and discussion

3.1. Calculation of interfacial-local electric field

To unravel the impact of an interfacial-local electric field construction on the d_z^2 occupancy for W-based catalysts, DFT calculations were initially performed. The model structures for C_3N_4 , WO_3 , and the WO_3 - C_3N_4 heterostructure are presented in Fig. S1 from various perspectives. The PDOS results revealed that a more potent interfacial-local electric field enhanced the d_z^2 occupancy of W (Figs. 1a and S2). Additionally, we observed an approximately linear relationship between d_z^2 occupancy and the interfacial-local electric field intensity (Fig. 1b). Crucially, the relationship between the change in Gibbs free energy during ENRR ($\Delta G_{N_2}^*$) and the interfacial-local electric field intensity manifested as a negative linear relationship (Fig. 1c). Notably, a lower $\Delta G_{N_2}^*$ corresponds to a more energetically favorable scenario for N_2 adsorption and activation, signifying a potential boost in ENRR efficiency. Therefore, the data indicate that the presence of a potent interfacial-local electric field could markedly elevate d_z^2 occupancy, consequently diminishing $\Delta G_{N_2}^*$ values. This scenario creates a beneficial environment for the adsorption and activation of N_2 , thereby enhancing ENRR performance.

To comprehend the formation mechanisms of interfacial and local electric fields within the WO_3 - C_3N_4 heterostructure, a series of in-depth

calculations were conducted. Firstly, to delineate the mechanism of interfacial electric field formation, we probed the electron transfer dynamics between WO_3 and C_3N_4 . The calculated work functions (WF) of C_3N_4 , WO_3 and WO_3 - C_3N_4 were 4.59, 3.54 and 4.16 eV (Fig. S3), respectively. These findings indicate that WO_3 has a smaller WF value, suggesting a predisposition for electron transfer from WO_3 to C_3N_4 [38, 39]. Furthermore, the difference in electrostatic potential energy between C_3N_4 and WO_3 was evaluated to substantiate the notion of electron transfer. As shown in Fig. 1d, the electron transfer potential (ΔV_{et}) in the C_3N_4 region is lower than that in the WO_3 regions, reinforcing that electron transfer from WO_3 to C_3N_4 is indeed energetically favorable. The difference in charge density (DCD) analysis was further performed to explore the electronic structure of WO_3 - C_3N_4 , showing an electron transfer of 0.69 e^- from WO_3 to C_3N_4 at the heterostructure interface (Fig. S4). In addition, the plane-averaged DCD in z-direction of WO_3 - C_3N_4 (Fig. 1e) clearly exhibits substantial charge transfer from WO_3 to C_3N_4 . The red and blue regions represent electron accumulation and depletion (Fig. 1e), respectively. Consequently, WO_3 and C_3N_4 become positively and negatively charged at the interface, respectively, resulting in a robust interfacial electric field directed from WO_3 to C_3N_4 [32,40]. Next, we sought to understand the local electric field formation within WO_3 - C_3N_4 by examining electron transfer dynamics among W active sites. As illustrated in Fig. 1f, W-N electron transfer channels are

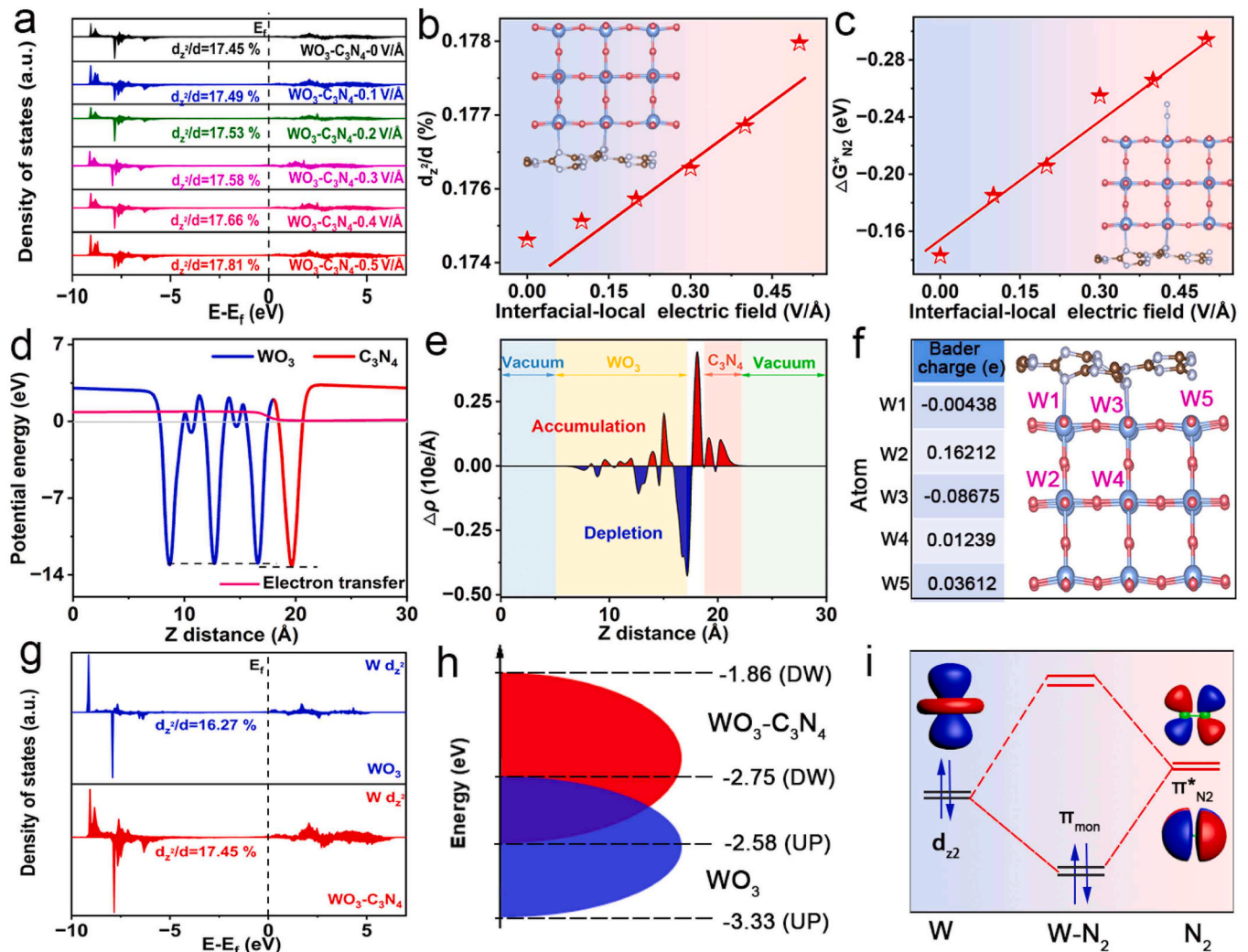


Fig. 1. (a) The PDOS of WO_3 - C_3N_4 and d_z^2/d values of the W active sites with different interfacial-local electric field intensities. (b) Relationship between d_z^2/d values and interfacial-local electric field intensities in WO_3 - C_3N_4 . (c) Relationship between $\Delta G_{N_2}^*$ values and interfacial-local electric field intensities in WO_3 - C_3N_4 . (d) The electrostatic potential profile of WO_3 - C_3N_4 . (e) Plane-averaged DCD for WO_3 - C_3N_4 . (f) Bader charges of W atoms in WO_3 - C_3N_4 . (g) The PDOS and (h) The W d_z^2 orbital energy level diagrams of WO_3 and WO_3 - C_3N_4 . (i) The schematic diagram of the electron transfer between W d_z^2 orbital and $\pi^*_{N_2}$ orbital.

present in the $\text{WO}_3\text{-C}_3\text{N}_4$ model. It is worth noting that negative and positive Bader charge values, represented in the inset table of Fig. 1f, signify the numbers of electron gains and losses at W active sites, respectively. Thus, an examination of charge density redistribution indicates that the presence of W-N bonds promotes electron loss at the W active sites connected to N, while simultaneously fostering electron enrichment at the around W active sites, thereby inducing an atomically local electric field. These findings form a comprehensive picture of the complex electron transfer dynamics within $\text{WO}_3\text{-C}_3\text{N}_4$ and their role in creating interfacial and local electric fields.

To further confirmed the initial hypothesis that an interfacial-local electric field augments the d_z^2 occupancy of W, PDOS was further performed to compare the d_z^2 occupancy between $\text{WO}_3\text{-C}_3\text{N}_4$ and WO_3 with results exhibiting that d_z^2 occupancy of $\text{WO}_3\text{-C}_3\text{N}_4$ (17.45%) is higher

than that of WO_3 (16.27%) (Fig. 1g and S5). Subsequently, an exploration of the variation in the d_z^2 orbital energy level in WO_3 and $\text{WO}_3\text{-C}_3\text{N}_4$ was carried out (Fig. 1h). The data revealed that $\text{WO}_3\text{-C}_3\text{N}_4$ showcased elevated spin down/up orbital energy levels of $-1.86\text{ eV}/-2.85\text{ eV}$, marking a notable increase compared to those of WO_3 ($-2.75\text{ eV}/-3.33\text{ eV}$). It is noteworthy to highlight that the raised d_z^2 orbital energy level in $\text{WO}_3\text{-C}_3\text{N}_4$ could potentially facilitate expedited electron transfer from W sites to N_2 (Fig. 1i). This enhanced transfer might bolster N_2 adsorption, thereby invigorating ENRR. Our comprehensive calculations have elucidated the generation mechanism underlying the interfacial-local electric field in the $\text{WO}_3\text{-C}_3\text{N}_4$ heterostructure. These in-depth analyses furnish compelling evidence in support of the notion that the presence of an interfacial-local electric field in the $\text{WO}_3\text{-C}_3\text{N}_4$ plays a crucial role in escalating the d_z^2 orbital energy level of W active sites,

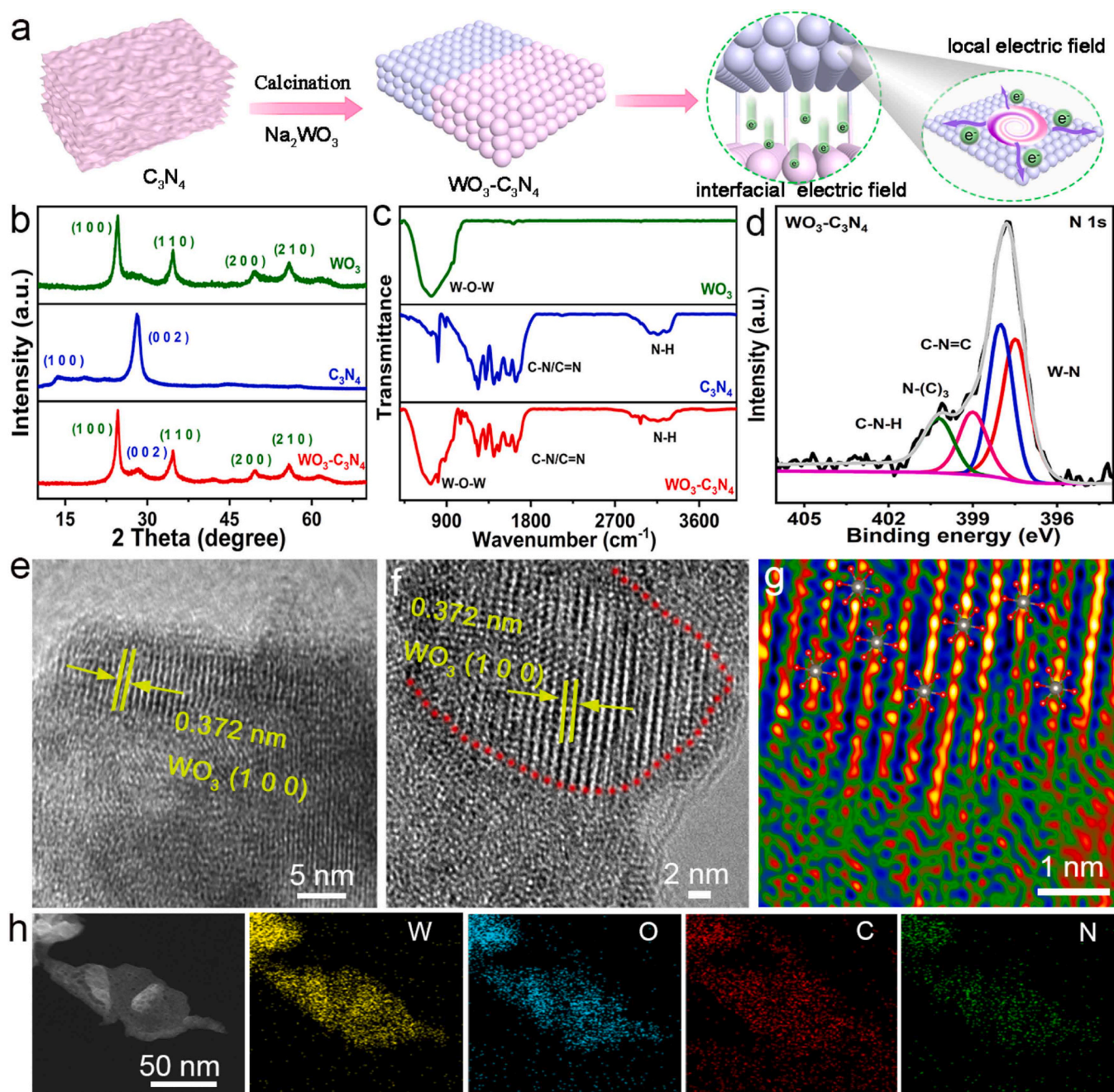


Fig. 2. (a) Synthesis schematic illustration of $\text{WO}_3\text{-C}_3\text{N}_4$. (b) XRD patterns and (c) FTIR spectra of all samples. (d) N 1s spectra of $\text{WO}_3\text{-C}_3\text{N}_4$. (e) HRTEM image and (f) HAADF-STEM image of $\text{WO}_3\text{-C}_3\text{N}_4$. (g) FFT patterns of $\text{WO}_3\text{-C}_3\text{N}_4$. (h) EDS elemental mapping images of $\text{WO}_3\text{-C}_3\text{N}_4$.

resulting in enhanced adsorption and activation processes of N_2 during ENRR.

3.2. Characterizations of WO_3 - C_3N_4 Materials

To confirm the above hypothesis, we successfully fabricated a WO_3 - C_3N_4 electrocatalyst through a facile method (Fig. 2a). For comparisons, the identical method was employed to construct WO_3 samples without the C_3N_4 , which was synthesized through the calcination of dicyandiamide (DICY). X-ray diffraction (XRD) test was conducted to decipher the crystal structure of the prepared samples [41]. Two peak values at 13.4° and 27.8° were discerned (Fig. 2b), correspondingly indicative of the (100) and (002) planes of C_3N_4 (JCPDS No. 87-1526). Concurrently, Peaks at 24.0° , 34.1° , 49.0° , and 55.3° (Fig. 2b) should be ascribed to the (100), (110), (200), and (210) planes of WO_3 (JCPDS No. 42-0905), respectively. To further investigate the surface functionalities of

samples, Fourier transform infrared (FTIR) spectroscopy was employed. Typical peaks within the range of 500 – 1000 cm^{-1} can be attributed to the stretching vibration of W-O-W in pure WO_3 (Fig. 2c). The pure C_3N_4 sample displayed a vibrational peak at 807 cm^{-1} (Fig. 2c), corresponding to the triazine vibrations. Furthermore, a series of peaks between 1200 and 1600 cm^{-1} were identified (Fig. 2c), attributable to C-N stretching vibrations. Broad peaks situated at 3000 – 3500 cm^{-1} were also observed (Fig. 2c), originating from N-H [42]. Most notably, we found the WO_3 - C_3N_4 heterostructure exhibited characteristic peaks of both WO_3 and C_3N_4 in both XRD and FTIR spectra, reinforcing the evidence for successful heterostructure formation. To explore the chemical compositions of all the materials, we carried out X-ray photoelectron spectroscopy (XPS). The N 1s spectrum of WO_3 - C_3N_4 (Fig. 2d) exhibits four peaks at 397.5 eV , 398.1 eV , 399.1 eV , and 400.2 eV , assigned to W-N, C-N = C, N-(C)₃, and C-N-H, respectively. The C 1s spectrum (Fig. S6a) shows two peaks at 284.8 eV and 288.7 eV , credited to C-C

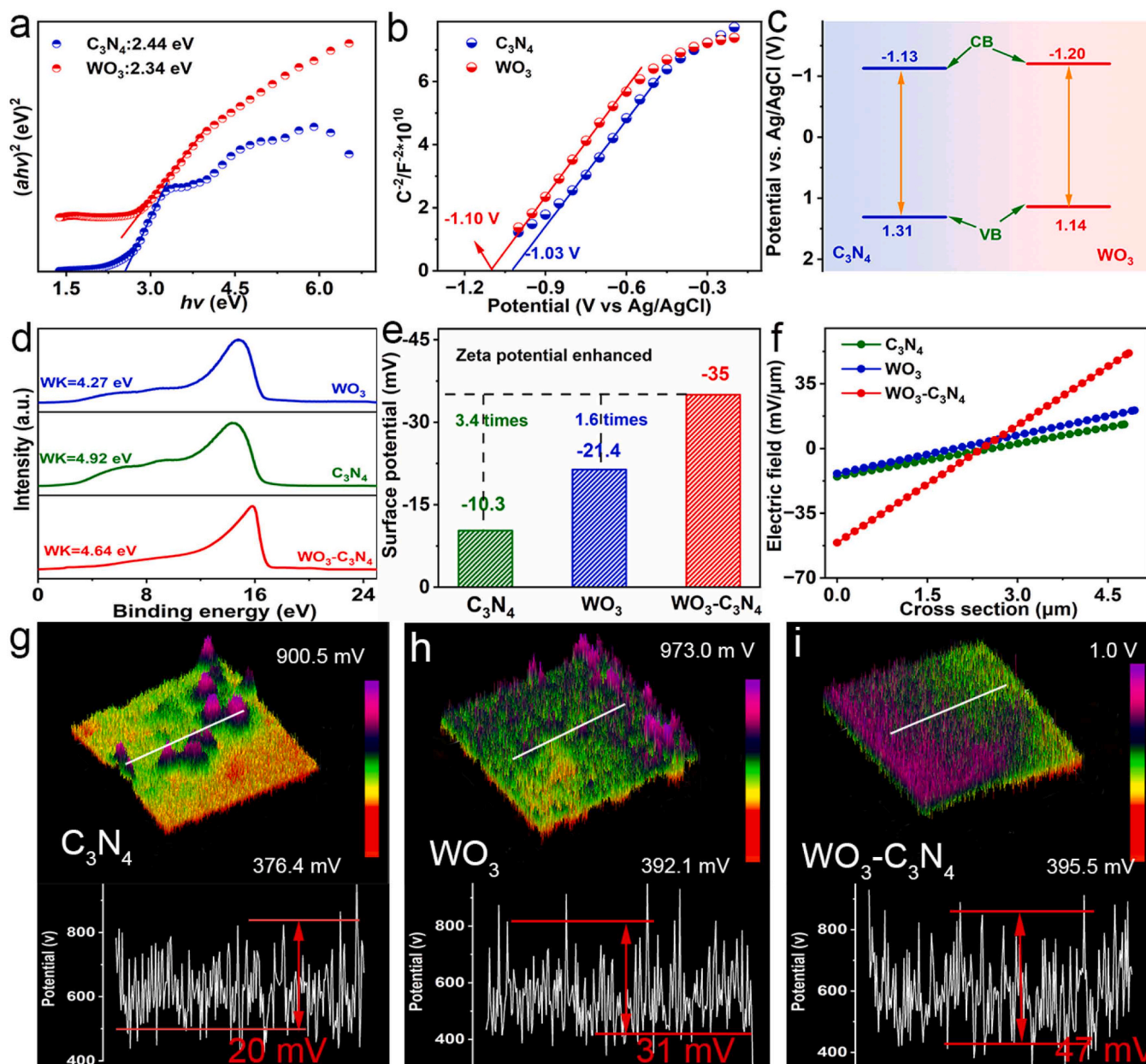


Fig. 3. (a) Kubelka-Munk plots and (b) Mott-Schottky plots of C_3N_4 and WO_3 . (c) The band structures of C_3N_4 and WO_3 . (d) UPS of C_3N_4 , WO_3 and WO_3 - C_3N_4 . (e) The zeta potential value of all samples. (f) The electric field intense distributions on all samples surfaces. 3D AFM images at the surface potential mode and corresponding potential profiles of (g) C_3N_4 , (h) WO_3 and (i) WO_3 - C_3N_4 .

and N = C-N. The W 4f spectrum of WO₃-C₃N₄ (Fig. S6b) shows peaks at 35.6 eV, 38.1 eV, and 41.8 eV, attributed to W 4f_{7/2}, W 4f_{5/2} and W 5p_{3/2} respectively. Compared to WO₃ (35.6, 37.8, and 41.3 eV), these peaks have shifted to higher energy regions, signifying electron transfer from WO₃ to C₃N₄, a result that aligns with DFT calculation results. Furthermore, peaks at 530.5 eV and 531.3 eV in the O 1s spectrum are designated as the lattice oxygen and adsorbed oxygen species in WO₃-C₃N₄ (Fig. S6c) [43,44]. The scanning electron microscopy (SEM) and transmission electron microscope (TEM) were further adopted to analyze the morphological characteristics of WO₃ and WO₃-C₃N₄. SEM and TEM imaging reveal both WO₃ and WO₃-C₃N₄ samples to be composed of sheet-like structures (Figs. S7 and S8). High-resolution TEM (HRTEM) images (Figs. 2e and S7c) unveil the lattice interplanar spacings of 0.372 nm, consistent with the (100) faces of WO₃. To dissect the architecture of WO₃-C₃N₄ at an even more refined level, high-angle annular dark-field scanning transmission electron microscopy (HAADF-STEM) was adopted with results showing clear interfaces between the WO₃ and C₃N₄ components (Fig. 2f). Complementing these images, fast Fourier transform (FFT) pattern of WO₃-C₃N₄ was acquired (Fig. 2g), elucidating the inherent WO₆ crystal characteristics of the WO₃ sheets. In addition, the elemental mapping exhibits a homogeneous distribution of W, O, C and N elements within the WO₃-C₃N₄ catalysts (Fig. 2h). Concurrently, Fig. S7d reveals a uniform dispersal of W and O elements within the WO₃ catalysts. Collectively, these meticulous investigations unequivocally confirm the successful synthesis of the WO₃-C₃N₄ heterostructure.

3.3. Characterizations of interfacial-local electric field

In an effort to rigorously establish the nature of electron transfer behavior in the WO₃-C₃N₄ heterostructure, a suite of experimental tools including UV/Vis diffuse reflectance spectra (DRS), the Mott-Schottky test, and ultraviolet photoelectron spectra (UPS) were employed. As reflected in Fig. 3a, the bandgaps for WO₃ and C₃N₄ were ascertained to be 2.34 eV and 2.44 eV, respectively [45]. The confluence of these findings with the conduction band positions of unadulterated WO₃ (−1.20 V) and C₃N₄ (−1.13 V) vs Ag/AgCl (Fig. 3b) serve to sketch the band structures (Fig. 3c) [46,47]. Moreover, the experimentally determined work function (WF) values for WO₃, C₃N₄, and the WO₃-C₃N₄ heterostructure were quantified to be 4.27 eV, 4.92 eV, and 4.64 eV respectively (Fig. 3d) [48,49]. Importantly, the coherence of all the experimental data underscores the predilection for electrons to readily transfer from the surface of WO₃ to C₃N₄, which is consistent with calculation results. To further substantiate the presence of an interfacial-local electric field within the WO₃-C₃N₄ heterostructure, an analysis of the zeta potential and surface potential distribution was carried out. The zeta potential of the WO₃-C₃N₄ heterostructure was found to be −35 mV (Fig. 3e), being 3.4 times and 1.6 times greater than that of C₃N₄ (−10.3 mV) and WO₃ (−21.4 mV) respectively [50–52]. Delving deeper, we employed differentiation of the fitting surface potential profiles (Fig. S9) to quantitatively characterize the electric field intensity. The derived electric field intensity of WO₃-C₃N₄ (Fig. 3f), attained a peak of 82 mV μm^{−1}, surpassing all other samples (C₃N₄ 20 mV μm^{−1} and WO₃ 75 mV μm^{−1}). In addition, examination of the three-dimensional (3D) AFM images at the surface potential mode for C₃N₄, WO₃, and WO₃-C₃N₄ (Fig. 3g-i) together with the corresponding lines-canning surface potential profiles, unveiled a higher contact potential difference (CPD) for WO₃-C₃N₄ (47 mV) relative to C₃N₄ (28 mV) and WO₃ (39 mV) [53,54]. Cumulatively, these results lend compelling support to the formation of a robust interfacial-local electric field within the WO₃-C₃N₄ heterostructure.

3.4. Electrocatalytic Activity for NRR

The ENRR experiments were conducted within a H-cell, partitioned by a Nafion 117 membrane at ambient temperature (Fig. S10). To gauge

the ENRR efficacy of the catalysts, linear sweep voltammetry (LSV) was assessed under both Ar and N₂ atmospheres (Fig. 4a). Intriguingly, under N₂ saturated conditions, WO₃-C₃N₄ registered a heightened current density relative to Ar saturated conditions, which strongly signals the progression of ENRR. Moreover, the absence of hydrazine (N₂H₄) in the electrolyte-as detected via the Watt-Chrisp method-points to an outstanding selectivity for ENRR (Fig. 4b and S11). Additionally, Fig. S13 displays no significant peaks associated with NO₂, which indicates the absence of nitrate contaminants during NRR. Further evidence was sought for the actual active sites within WO₃-C₃N₄ through a poisoning experiment employing SCN[−] ions. Fig. 4c displays a reduction in ENRR activity on WO₃-C₃N₄ post SCN[−] ion injection, indicative of active site blockage, corroborating the role of W as active sites for ENRR [55,56]. Subsequent to this, chronoamperometry measurements and UV–vis absorption spectra were deployed to comprehensively scrutinize the ENRR activity (Figs. S12 and S14 and 15). As depicted in Fig. 4d and e, WO₃-C₃N₄ attains a pinnacle NH₃ yield rate and Faradaic efficiency (FE) of 54.87 μg h^{−1} mg_{cat}^{−1} and 24.33%, outstripping those of WO₃ (44.27 μg h^{−1} mg_{cat}^{−1} and 15.58%), respectively. This remarkable ENRR performance, concurrent at a low potential, eclipses much of the previously reported work (Fig. 4f and Table S1). Importantly, the WO₃-C₃N₄ demonstrates robust stability across five cycles, presenting no significant fluctuation in the NH₃ yield rate and FE (Fig. S16). Subsequent XRD and SEM analyses were carried out to confirm the structural stability of the materials. The results indicate that the WO₃-C₃N₄ exhibited no discernible structural changes following the ENRR, thereby demonstrating its excellent structural durability (Fig. S17).

To assert with certainty that the NH₃ present in the electrolyte originated from ENRR, several control experiments and a ¹⁵N isotope labeling experiment were conducted. As delineated in Fig. 4g, the control experiments bore no significant NH₃ generation. Intriguingly, the ¹H nuclear magnetic resonance (¹H NMR) spectra (Fig. 4h) manifested a double coupling and a triplet coupling corresponding to ¹⁵NH₄⁺ and ¹⁴NH₄⁺ when utilizing ¹⁵N₂ and ¹⁴N₂ as gas supply, respectively. This strongly suggests the feeding gas as the sole N source. Furthermore, to corroborate the elevated ENRR performance of WO₃-C₃N₄, electrochemical active surface area (ECSA) was measured. ECSA was assessed by determining the double-layer capacitance (C_{dl}) (Fig. 4i and S18). The calculated C_{dl} values for WO₃-C₃N₄ were determined to be 0.011 mF cm^{−2}, which is notably lower than those of WO₃ and C₃N₄, with values of 0.037 mF cm^{−2} and 0.021 mF cm^{−2} (Fig. S18), respectively. Concurrently, WO₃-C₃N₄ exhibited the highest turnover frequency (TOF) among the studied catalysts, achieving a value of 16.36 h^{−1}. This TOF is significantly higher than those of C₃N₄ and WO₃, surpassing them by 7.94-fold and 4.06-fold (Fig. S19), respectively. This implies that the WO₃-C₃N₄ harbors smaller active sites. Nevertheless, the NH₃ yield of the WO₃-C₃N₄ electrocatalyst surpassed that of WO₃, implying that the ECSA is not the prime factor for ENRR[57]. Furthermore, electrochemical impedance spectroscopy (EIS) analyses were conducted, revealing that the WO₃-C₃N₄ exhibits a lower charge transfer resistance (R_{ct}) value of 105.4 Ω, in comparison to that of WO₃, which is 582.8 Ω (Fig. S20). This significant difference highlights the superior charge transfer kinetics of the WO₃-C₃N₄. Instead, this enhancement in ENRR performance could be attributed to the influence of the interfacial-local electric field.

3.5. In situ measurements and DFT calculation

The adsorptive capacity of electrocatalysts for nitrogen (N₂) was scrutinized through nitrogen temperature-programmed desorption (N₂-TPD). Fig. 5a manifests a more elevated N₂-desorption peak temperature for WO₃-C₃N₄ (501.4 °C), compared to the WO₃ (264.1 °C). This disparity signifies a higher binding affinity for N₂ on WO₃-C₃N₄ than on WO₃. The interplay between N₂ and the catalyst was further explored through *in situ* Raman and FTIR. Fig. 5b portrays a prominent peak at 800 cm^{−1} corresponding to W-N vibrational band for WO₃-C₃N₄, absent

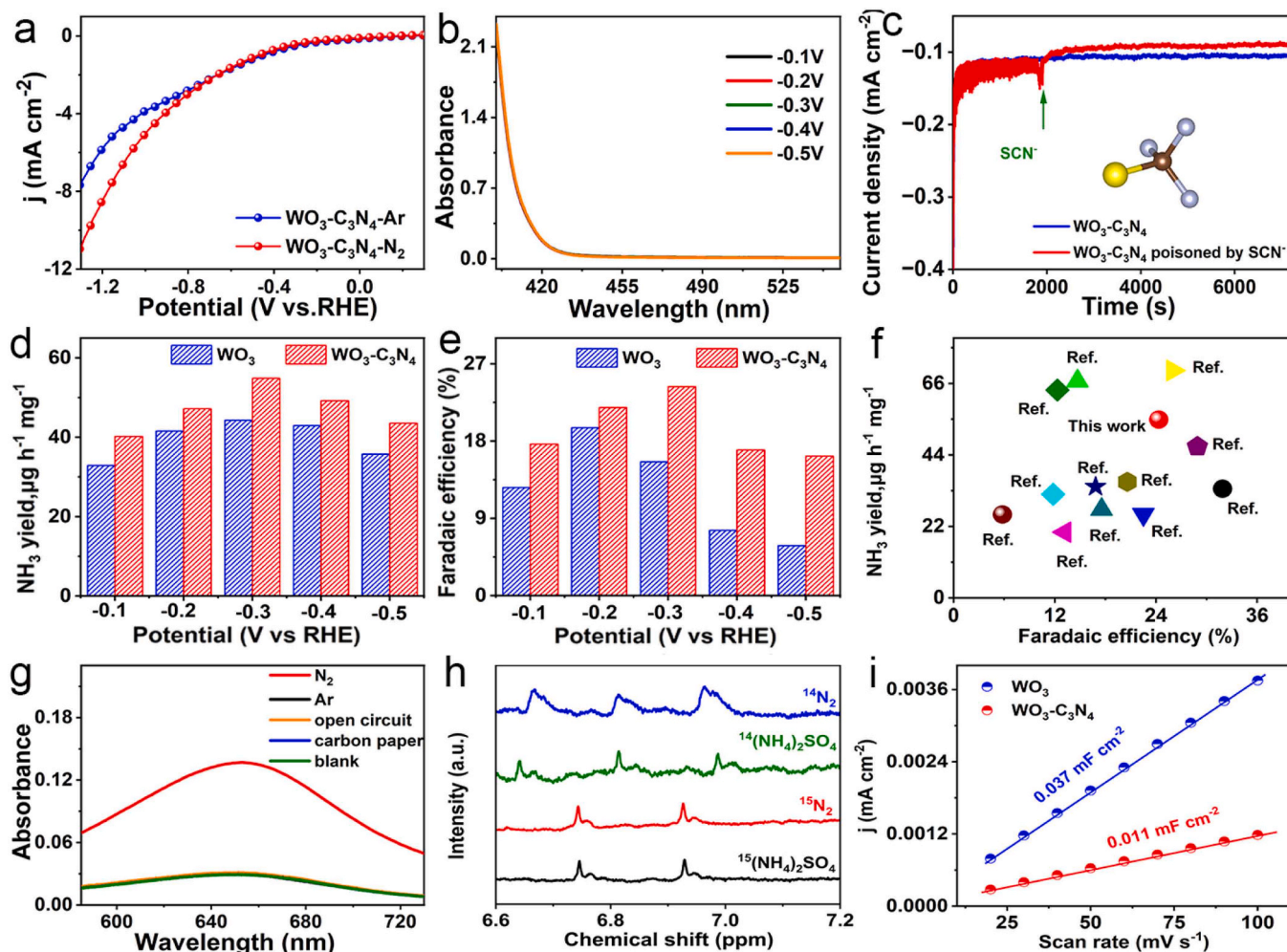


Fig. 4. (a) LSV curves of $\text{WO}_3\text{-C}_3\text{N}_4$ under different atmosphere (N_2 and Ar) in 0.1 M Li_2SO_4 . (b) Hydrazine hydrate detection after electrolysis. (c) Chronoamperometry curves (-0.3 V) under N_2 atmosphere for $\text{WO}_3\text{-C}_3\text{N}_4$ with *in situ* addition of SCN^- . (d) NH_3 yield and (e) Faradaic efficiency of WO_3 and $\text{WO}_3\text{-C}_3\text{N}_4$. (f) Comparison of ENRR performance of $\text{WO}_3\text{-C}_3\text{N}_4$ with other reported catalysts (Table S1). (g) UV-vis absorption spectra under different control experiments. (h) ^1H NMR spectra of $\text{WO}_3\text{-C}_3\text{N}_4$ fed by $^{14}\text{N}_2$ and $^{15}\text{N}_2$ gas. (i) C_{dl} measurements of WO_3 and $\text{WO}_3\text{-C}_3\text{N}_4$.

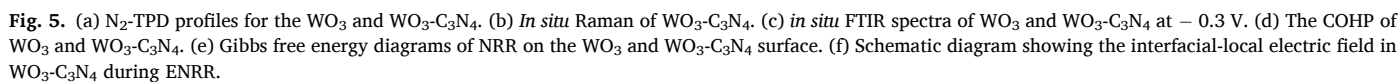
in WO_3 (Fig. S21), indicating that N_2 molecules have a higher propensity to adsorb onto the W active sites of $\text{WO}_3\text{-C}_3\text{N}_4$ [16]. Supporting this finding, an "acceptance-donation" mechanism is proposed (Fig. S22), whereby the vacant d orbitals of W atom engage with the lone-pair electrons of the N_2 molecule. This interaction permits the occupied d orbital to share electrons with the π^* orbital of N_2 , thereby attenuating the $\text{N}\equiv\text{N}$ bond and setting the stage for N_2 activation, expediting its transformation into NH_3 . In addition, Fig. 5c exhibits a noteworthy blueshift in the nitrogen adsorption peak for $\text{WO}_3\text{-C}_3\text{N}_4$ (1228 cm^{-1}), in comparison to WO_3 (1260 cm^{-1}). This shift implies an elongation of the $\text{N}\equiv\text{N}$ bond upon N_2 adsorption onto the $\text{WO}_3\text{-C}_3\text{N}_4$ surface [18]. These collective observations posit the possibility of an intensified interfacial-local electric field instigating a surge in d_z^2 occupancy of W active sites. This, in turn, would bolster both the adsorption and subsequent activation of N_2 molecules.

Further insights into the superior ENRR performance of $\text{WO}_3\text{-C}_3\text{N}_4$ are gleaned through crystal orbital Hamilton population (COHP) analysis (Fig. 5d). Integrated COHP (ICOHP) values for the W-N bond in WO_3 and $\text{WO}_3\text{-C}_3\text{N}_4$ are calculated to be -1.24 and -1.47 , respectively. A greater absolute value implies a stronger W-N bond in $\text{WO}_3\text{-C}_3\text{N}_4$ relative to WO_3 . Simultaneously, the ICOHP value for the N-N bond in $\text{WO}_3\text{-C}_3\text{N}_4$ is found to be -1.53 , lower than WO_3 (-2.40) [58–60]. This finding points to the effectiveness of an elevated d_z^2 occupancy of W sites in $\text{WO}_3\text{-C}_3\text{N}_4$ at weakening the $\text{N}\equiv\text{N}$ bond. An NRR free-energy diagram

further substantiates the superior ENRR performance of $\text{WO}_3\text{-C}_3\text{N}_4$. As evidenced in Fig. 5e, $\text{WO}_3\text{-C}_3\text{N}_4$ presents a negative free energy (-0.14 eV) of N_2 adsorption and a lower energy barrier (0.891 eV) for the rate-limiting step (RDS), transitioning from $^*\text{N-N}$ to $^*\text{NNH}$, when compared with WO_3 (0.48 eV and RDS of 0.935 eV , respectively). This indicates that $\text{WO}_3\text{-C}_3\text{N}_4$, with an elevated d_z^2 occupancy of W sites, is capable of effectively activating the $\text{N}\equiv\text{N}$ bond and diminishing the RDS energy barrier. Optimized configurations of intermediates are presented in Figs. 5e and S23. Further investigations were conducted to elucidate the electrocatalytic hydrogen evolution reaction (HER) behavior of the catalysts. As shown in Fig. S24, $\text{WO}_3\text{-C}_3\text{N}_4$ features a higher reaction energy barrier (1.18 eV) compared to WO_3 (0.96 eV). This evidence suggests that $\text{WO}_3\text{-C}_3\text{N}_4$ could effectively suppress the competing HER. Collectively, these computational results reinforce that $\text{WO}_3\text{-C}_3\text{N}_4$, with an elevated d_z^2 occupancy of W active sites, promotes the adsorption and activation of N_2 on the electrocatalyst surface, thus enhancing ENRR performance. Fig. 5f provides a schematic diagram to further illustrate the role of the interfacial-local electric field on $\text{WO}_3\text{-C}_3\text{N}_4$, and how it may bolster ENRR performance by effectively increasing d_z^2 occupancy of W active sites.

4. Conclusion

In conclusion, this work highlights the ability of the $\text{WO}_3\text{-C}_3\text{N}_4$



Yan Yi-Ming: Funding acquisition, Writing – review & editing. **Li Jingxian:** Investigation. **Yang Zhiyu:** Writing – review & editing. **Wang Xiaoxuan:** Data curation, Formal analysis, Writing – original draft, Writing – review & editing. **Li Shuyuan:** Investigation. **Ji Yingjie:** Investigation. **Zhang Huiying:** Investigation. **Tang Zheng:** Investigation. **Xie Jiangzhou:** Writing – review & editing. **Zhang Feike:**

Investigation. **Wang Shiyu:** Investigation. **Gao Xueying:** Investigation. **Sun Yanfei:** Investigation.

Declaration of Competing Interest

The authors declare that they have no known competing financial interests or personal relationships that could have appeared to influence the work reported in this paper.

Data availability

Data will be made available on request.

Acknowledgements

Financial support from the National Natural Science Foundation of China (grant nos. 21575016, U20A20154, 22379006, 22279005) and from the National Program for Support of Top-notch Young Professionals is gratefully acknowledged. We thank the Hefei Advanced Computing Center.

Appendix A. Supporting information

Supplementary data associated with this article can be found in the online version at [doi:10.1016/j.apcatb.2024.123700](https://doi.org/10.1016/j.apcatb.2024.123700).

References

- [1] R. Liu, H. Fei, J. Wang, T. Guo, F. Liu, J. Wang, Z. Wu, D. Wang, Insights of active sites separation mechanism for highly efficient electrocatalytic N₂ reduction to ammonia over glucose-induced metallic MoS₂, *Appl. Catal. B Environ.* 337 (2023) 122997, <https://doi.org/10.1016/j.apcatb.2023.122997>.
- [2] X. Wang, J. Xie, S. Li, Z. Yuan, Y. Sun, X. Gao, Z. Tang, H. Zhang, J. Li, S. Wang, Z. Yang, Y.-M. Yan, Enhancing interfacial electric field in WO₃-C₃N₄ through fermi level modulation for electrocatalytic nitrogen reduction, *Appl. Catal. B Environ.* 339 (2023) 123126, <https://doi.org/10.1016/j.apcatb.2023.123126>.
- [3] H.Y. Zhou, Y.B. Qu, Y.C. Fan, Z.L. Wang, X.Y. Lang, J.C. Li, Q. Jiang, Multi-site intermetallic Ni₃Mo effectively boosts selective ammonia synthesis, *Appl. Catal. B Environ.* 339 (2023) 123133, <https://doi.org/10.1016/j.apcatb.2023.123133>.
- [4] M. Kim, J. Chung, T. An, J. Lee, M. Han, S. Lee, W. Choi, J. Kim, S. Han, U. Sim, T. Y. Yu, Paradox of thiourea: a false-positive and promoter for electrochemical nitrogen reduction on nickel sulfide catalysts, *Appl. Catal. B Environ.* 328 (2023) 122485, <https://doi.org/10.1016/j.apcatb.2023.122485>.
- [5] X. Feng, J. Liu, L. Chen, Y. Kong, Z. Zhang, Z. Zhang, D. Wang, W. Liu, S. Li, L. Tong, J. Zhang, Hydrogen radical-induced electrocatalytic N₂ reduction at a low potential, *J. Am. Chem. Soc.* 145 (2023) 10259–10267, <https://doi.org/10.1021/jacs.3c01319>.
- [6] X.C. Gao-Feng Chen, Shunqing Wu, Xingye Zeng, Liang-Xin Ding, Min Zhu, Haihui Wang, Ammonia electrosynthesis with high selectivity under ambient conditions via a Li⁺ incorporation strategy, *J. Am. Chem. Soc.* 139 (2017) 9771–9774, <https://doi.org/10.1021/jacs.7b04393>.
- [7] B. Mishra, S. Biswal, M. Ussama, M. Ali Haider, B.P. Tripathi, Rationally designed oxygen vacant TiO₂ decorated with covalent organic framework for enhanced electrocatalytic nitrogen reduction to ammonia, *Appl. Catal. B Environ.* 342 (2024) 123395, <https://doi.org/10.1016/j.apcatb.2023.123395>.
- [8] P. Li, Y. Lin, Z. Qi, D. Yan, Efficient photoelectrocatalytic CO₂ reduction to CH₃OH via porous g-C₃N₄ nanosheets modified with cobalt phthalocyanine in ionic liquids, *J. Mater. Chem. A* 11 (2023) 21078–21088, <https://doi.org/10.1039/d3ta03285j>.
- [9] P. Li, T. Zhang, M.A. Mushtaq, S. Wu, X. Xiang, D. Yan, Research progress in organic synthesis by means of photoelectrocatalysis, *Chem. Rec.* 21 (2021) 841–857, <https://doi.org/10.1002/tcr.202000186>.
- [10] Z. Guo, W. Ye, X. Fang, J. Wan, Y. Ye, Y. Dong, D. Cao, D. Yan, Amorphous cobalt-iron hydroxides as high-efficiency oxygen-evolution catalysts based on a facile electrospinning process, *Inorg. Chem. Front.* 6 (2019) 687–693, <https://doi.org/10.1039/c8qi01320a>.
- [11] M.A. Mushtaq, M. Arif, G. Yasin, M. Tabish, A. Kumar, S. Ibraheem, W. Ye, S. Ajmal, J. Zhao, P. Li, J. Liu, A. Saad, X. Fang, X. Cai, S. Ji, D. Yan, Recent developments in heterogeneous electrocatalysts for ambient nitrogen reduction to ammonia: activity, challenges, and future perspectives, *Renew. Sustain. Energy Rev.* 176 (2023) 113197, <https://doi.org/10.1016/j.rser.2023.113197>.
- [12] M.A. Mushtaq, A. Kumar, G. Yasin, M. Arif, M. Tabish, S. Ibraheem, X. Cai, W. Ye, X. Fang, A. Saad, J. Zhao, S. Ji, D. Yan, 3D interconnected porous Mo-doped WO₃@CdS hierarchical hollow heterostructures for efficient photoelectrochemical nitrogen reduction to ammonia, *Appl. Catal. B Environ.* 317 (2022) 121711, <https://doi.org/10.1016/j.apcatb.2022.121711>.
- [13] P. Li, Y. Liu, M.A. Mushtaq, D. Yan, Recent progress in ammonia synthesis based on photoelectrocatalysis, *Inorg. Chem. Front.* 10 (2023) 4650–4667, <https://doi.org/10.1039/d3qi00683b>.
- [14] D. Ye, S.C.E. Tsang, Prospects and challenges of green ammonia synthesis, *Nat. Synth.* 2 (2023) 612–623, <https://doi.org/10.1038/s44160-023-00321-7>.
- [15] L. Zhang, H. Zhou, X. Yang, S. Zhang, H. Zhang, X. Yang, X. Su, J. Zhang, Z. Lin, Boosting electroreduction kinetics of nitrogen to ammonia via atomically dispersed Sn protuberance, *Angew. Chem. Int. Ed.* 62 (2023) e202217473, <https://doi.org/10.1002/anie.202217473>.
- [16] Z. Yao, S. Liu, H. Liu, Y. Ruan, S. Hong, T.S. Wu, L. Hao, Y.L. Soo, P. Xiong, M.M. J. Li, A.W. Robertson, Q. Xia, L.X. Ding, Z. Sun, Pre-adsorbed H-assisted N₂ activation on single-atom cadmium-O₅ decorated In₂O₃ for efficient NH₃ electrosynthesis, *Adv. Funct. Mater.* 33 (2022) 2209843, <https://doi.org/10.1002/adfm.202209843>.
- [17] X. Guo, J. Gu, S. Lin, S. Zhang, Z. Chen, S. Huang, Tackling the activity and selectivity challenges of electrocatalysts toward the nitrogen reduction reaction via atomically dispersed biatom catalysts, *J. Am. Chem. Soc.* 142 (2020) 5709–5721, <https://doi.org/10.1021/jacs.9b13349>.
- [18] H. Li, M. Xia, B. Chong, H. Xiao, B. Zhang, B. Lin, B. Yang, G. Yang, Boosting photocatalytic nitrogen fixation via constructing low-oxidation-state active sites in the nanoconfined spinel iron cobalt oxide, *ACS Catal.* 12 (2022) 10361–10372, <https://doi.org/10.1021/acscatal.2c02282>.
- [19] X. Li, P. Shen, Y. Luo, Y. Li, Y. Guo, H. Zhang, K. Chu, PdFe single-atom alloy metallene for N₂ electroreduction, *Angew. Chem. Int. Ed.* 61 (2022) e202205923, <https://doi.org/10.1002/anie.202205923>.
- [20] Tongwei Wu, Marko M. Melander, K. Honkala, Coadsorption of NRR and HER intermediates determines the performance of Ru-N₄ toward electrocatalytic N₂ reduction, *ACS Catal.* 12 (2022) 2505–2512, <https://doi.org/10.1021/acscatal.1c05820>.
- [21] K. Chu, Y. Luo, P. Shen, X. Li, Q. Li, Y. Guo, Unveiling the synergy of O-vacancy and heterostructure over MoO_{3-x}/MXene for N₂ electroreduction to NH₃, *Adv. Energy Mater.* 12 (2021) 2103022, <https://doi.org/10.1002/aenm.202103022>.
- [22] J. Han, P. An, S. Liu, X. Zhang, D. Wang, Y. Yuan, J. Guo, X. Qiu, K. Hou, L. Shi, Y. Zhang, S. Zhao, C. Long, Z. Tang, Reordering d orbital energies of single-site catalysts for CO₂ electroreduction, *Angew. Chem. Int. Ed.* 58 (2019) 12711–12716, <https://doi.org/10.1002/anie.201907399>.
- [23] Y. Dai, B. Liu, Z. Zhang, P. Guo, C. Liu, Y. Zhang, L. Zhao, Z. Wang, Tailoring the d-orbital splitting manner of single atomic sites for enhanced oxygen reduction, *Adv. Mater.* 35 (2023) 2210757, <https://doi.org/10.1002/adma.202210757>.
- [24] M. Xiao, J. Zhu, S. Li, G. Li, W. Liu, Y.-P. Deng, Z. Bai, L. Ma, M. Feng, T. Wu, D. Su, J. Lu, A. Yu, Z. Chen, 3d-orbital occupancy regulated Ir-Co atomic pair toward superior bifunctional oxygen electrocatalysis, *ACS Catal.* 11 (2021) 8837–8846, <https://doi.org/10.1021/acscatal.1c02165>.
- [25] F.Y. Gao, S.J. Hu, X.L. Zhang, Y.R. Zheng, H.J. Wang, Z.Z. Niu, P.P. Yang, R.C. Bao, T. Ma, Z. Dang, Y. Guan, X.S. Zheng, X. Zheng, J.F. Zhu, M.R. Gao, S.H. Yu, High-curvature transition-metal chalcogenide nanostructures with a pronounced proximity effect enable fast and selective CO₂ electroreduction, *Angew. Chem. Int. Ed.* 59 (2020) 8706–8712, <https://doi.org/10.1002/anie.201912348>.
- [26] Y. Lv, R. Yuan, B. Cai, B. Bahrami, A.H. Chowdhury, C. Yang, Y. Wu, Q. Qiao, S. Liu, W.H. Zhang, High-efficiency perovskite solar cells enabled by anatase TiO₂ nanopyramidal arrays with an oriented electric field, *Angew. Chem. Int. Ed.* 59 (2020) 11969–11976, <https://doi.org/10.1002/anie.201915928>.
- [27] M. Liu, Y. Pang, B. Zhang, P. De Luna, O. Voznyy, J. Xu, X. Zheng, C.T. Dinh, F. Fan, C. Cao, F.P. de Arquer, T.S. Saeedi, A. Mephram, A. Klinkova, E. Kumacheva, T. Filletier, D. Sinton, S.O. Kelley, E.H. Sargent, Enhanced electrocatalytic CO₂ reduction via field-induced reagent concentration, *Nature* 537 (2016) 382–386, <https://doi.org/10.1038/nature19060>.
- [28] X. Wang, L. Zhao, R. Zhao, Y. Zhou, S. Wang, X. Chi, Y. Xiong, Y. Yao, K. Zhang, Y. Li, Z. Yang, Y.-M. Yan, Enhanced electrocatalytic nitrogen reduction inspired by a lightning rod effect on urchin-like Co₃O₄ catalyst, *Chem. Eng. J.* 450 (2022), <https://doi.org/10.1016/j.cej.2022.138316>.
- [29] C. Yan, Y. Zhu, Y. Li, Z. Fang, L. Peng, X. Zhou, G. Chen, G. Yu, Local built-in electric field enabled in carbon-doped Co₃O₄ nanocrystals for superior lithium-ion storage, *Adv. Funct. Mater.* 28 (2018) 1705951, <https://doi.org/10.1002/adfm.201705951>.
- [30] C. Cai, B. Liu, K. Liu, P. Li, J. Fu, Y. Wang, W. Li, C. Tian, Y. Kang, A. Stefancu, H. Li, C.W. Kao, T.S. Chan, Z. Lin, L. Chai, E. Cortés, M. Liu, Heteroatoms induce localization of the electric field and promote a wide potential-window selectivity towards CO in the CO₂ electroreduction, *Angew. Chem. Int. Ed.* 61 (2022) e202212640, <https://doi.org/10.1002/anie.202212640>.
- [31] X.X. Wang, S.Y. Li, Z. Yuan, Y.F. Sun, Z. Tang, X.Y. Gao, H.Y. Zhang, J.X. Li, S. Y. Wang, D.C. Yang, J.Z. Xie, Z.Y. Yang, Y.-M. Yan, Optimizing electrocatalytic nitrogen reduction via interfacial electric field modulation: elevating d-band center in WS₂-WO₃ for enhanced intermediate adsorption, *Angew. Chem. Int. Ed.* 62 (2023) e202303794, <https://doi.org/10.1002/anie.202303794>.
- [32] M. Yuan, J. Chen, Y. Bai, Z. Liu, J. Zhang, T. Zhao, Q. Wang, S. Li, H. He, G. Zhang, Unveiling electrochemical urea synthesis by Co-activation of CO₂ and N₂ with Mott-Schottky heterostructure catalysts, *Angew. Chem. Int. Ed.* 60 (2021) 10910–10918, <https://doi.org/10.1002/anie.202101275>.
- [33] Y. Liu, Y. Chen, Y. Tian, T. Sakthivel, H. Liu, S. Guo, H. Zeng, Z. Dai, Synergizing hydroxide spillover and deprotonation by the internal polarization field in a MoS₂/NiPS₃ vertical heterostructure for boosted water electrolysis, *Adv. Mater.* 34 (2022) e2203615, <https://doi.org/10.1002/adma.202203615>.
- [34] Z. Zhu, Q. Lv, Y. Ni, S. Gao, J. Geng, J. Liang, F. Li, Internal electric field and interfacial bonding engineered step-scheme junction for a visible-light-involved

- lithium-oxygen battery, *Angew. Chem. Int. Ed.* 61 (2022) e202116699, <https://doi.org/10.1002/anie.202116699>.
- [35] H. Choi, S. Surendran, Y. Sim, M. Je, G. Janani, H. Choi, J.K. Kim, U. Sim, Enhanced electrocatalytic full water-splitting reaction by interfacial electric field in 2D/2D heterojunction, *Chem. Eng. J.* 450 (2022) 137789, <https://doi.org/10.1016/j.cej.2022.137789>.
- [36] L. Zhai, X. She, L. Zhuang, Y. Li, R. Ding, X. Guo, Y. Zhang, Y. Zhu, K. Xu, H.J. Fan, S.P. Lau, Modulating built-in electric field via variable oxygen affinity for robust hydrogen evolution reaction in neutral media, *Angew. Chem. Int. Ed.* 61 (2022) e202116057, <https://doi.org/10.1002/anie.202116057>.
- [37] X.X. Wang, X.Y. Chi, Z.Z. Fu, Y.Y. Xiong, S.Y. Li, Y.B. Yao, K.X. Zhang, Y.J. Li, S. Y. Wang, R. Zhao, Z.Y. Yang, Y.-M. Yan, Interfacial electric field triggered N_2 activation for efficient electrochemical synthesis of ammonia, *Appl. Catal. B Environ.* 322 (2023) 122130, <https://doi.org/10.1016/j.apcatb.2022.122130>.
- [38] Y. Zhou, Y. Yao, R. Zhao, X. Wang, Z. Fu, D. Wang, H. Wang, L. Zhao, W. Ni, Z. Yang, Y.M. Yan, Stabilization of Cu^+ via strong electronic interaction for selective and stable CO_2 electroreduction, *Angew. Chem. Int. Ed.* 61 (2022) e202205832, <https://doi.org/10.1002/anie.202205832>.
- [39] L. Lv, X. He, J. Wang, Y. Ruan, S. Ouyang, H. Yuan, T.R. Zhang, Charge localization to optimize reactant adsorption on KCu_2S_4/CuO interfacial structure toward selective CO_2 electroreduction, *Appl. Catal. B Environ.* 298 (2021) 120531, <https://doi.org/10.1016/j.apcatb.2021.120531>.
- [40] Z. Zhu, Q. Lv, Y. Ni, S. Gao, J. Geng, J. Liang, F. Li, Internal electric field and interfacial bonding engineered step-scheme junction for a visible-light-involved lithium-oxygen battery, *Angew. Chem. Int. Ed.* 61 (2022), <https://doi.org/10.1002/anie.202116699>.
- [41] J. Fu, Q. Xu, J. Low, C. Jiang, J. Yu, Ultrathin 2D/2D $WO_3/g-C_3N_4$ step-scheme H_2 -production photocatalyst, *Appl. Catal. B Environ.* 243 (2019) 556–565, <https://doi.org/10.1016/j.apcatb.2018.11.011>.
- [42] K. Chu, Y.P. Liu, Y.B. Li, Y.L. Guo, Y. Tian, Two-dimensional (2D)/2D interface engineering of a MoS_2/C_3N_4 heterostructure for promoted electrocatalytic nitrogen fixation, *ACS Appl. Mater. Interfaces* 12 (2020) 7081–7090, <https://doi.org/10.1021/acsami.9b18263>.
- [43] Z.-Y. Liang, J.-X. Wei, X. Wang, Y. Yu, F.-X. Xiao, Elegant Z-scheme-dictated $g-C_3N_4$ enwrapped WO_3 superstructures: a multifarious platform for versatile photoredox catalysis, *J. Mater. Chem. A* 5 (2017) 15601–15612, <https://doi.org/10.1039/c7ta04333c>.
- [44] Y. Zhang, Z. Gu, J. Bi, Y. Jiao, Molybdenum-iron-cobalt oxyhydroxide with rich oxygen vacancies for the oxygen evolution reaction, *Nanoscale* 14 (2022) 10873–10879, <https://doi.org/10.1039/d2nr02568j>.
- [45] Z. Zhu, H. Huang, L. Liu, F. Chen, N. Tian, Y. Zhang, H. Yu, Chemically bonded $\alpha-Fe_2O_3/Bi_4MO_8Cl$ dot-on-plate Z-scheme junction with strong internal electric field for selective photo-oxidation of aromatic alcohols, *Angew. Chem. Int. Ed.* 61 (2022) e202203519, <https://doi.org/10.1002/anie.202203519>.
- [46] Y. Lin, C. Yang, S. Wu, X. Li, Y. Chen, W.L. Yang, Construction of built-in electric field within silver phosphate photocatalyst for enhanced removal of recalcitrant organic pollutants, *Adv. Funct. Mater.* 30 (2020) 2002918, <https://doi.org/10.1002/adfm.202002918>.
- [47] C. Lv, C. Yan, G. Chen, Y. Ding, J. Sun, Y. Zhou, G. Yu, An amorphous noble-metal-free electrocatalyst that enables nitrogen fixation under ambient conditions, *Angew. Chem. Int. Ed.* 57 (2018) 6073–6076, <https://doi.org/10.1002/anie.201801538>.
- [48] Q. Meng, C. Lv, J. Sun, W. Hong, W. Xing, L. Qiang, G. Chen, X. Jin, High-efficiency Fe-mediated Bi_2MoO_6 nitrogen-fixing photocatalyst: reduced surface work function and ameliorated surface reaction, *Appl. Catal. B Environ.* 256 (2019) 117781, <https://doi.org/10.1016/j.apcatb.2019.117781>.
- [49] X. Zhao, X. Li, L. An, L. Zheng, J. Yang, D. Wang, Controlling the valence-electron arrangement of nickel active centers for efficient hydrogen oxidation electrocatalysis, *Angew. Chem. Int. Ed.* 61 (2022) e202206588, <https://doi.org/10.1002/anie.202206588>.
- [50] Y. Guo, W. Shi, Y. Zhu, Y. Xu, F. Cui, Enhanced photoactivity and oxidizing ability simultaneously via internal electric field and valence band position by crystal structure of bismuth oxyiodide, *Appl. Catal. B Environ.* 262 (2020) 118262, <https://doi.org/10.1016/j.apcatb.2019.118262>.
- [51] Z. Xing, J. Hu, M. Ma, H. Lin, Y. An, Z. Liu, Y. Zhang, J. Li, S. Yang, From one to two: in situ construction of an ultrathin $^2D-^2D$ closely bonded heterojunction from a single-phase monolayer nanosheet, *J. Am. Chem. Soc.* 141 (2019) 19715–19727, <https://doi.org/10.1021/jacs.9b08651>.
- [52] J. Zheng, Y. Lyu, M. Qiao, J.P. Veder, R.D. Marco, J. Bradley, R. Wang, Y. Li, A. Huang, S.P. Jiang, S. Wang, Tuning the electron localization of gold enables the control of nitrogen-to-ammonia fixation, *Angew. Chem. Int. Ed.* 58 (2019) 18604–18609, <https://doi.org/10.1002/anie.201909477>.
- [53] C. Wang, Y. Liu, Z. Li, L. Wang, X. Niu, P. Sun, Novel space-confinement synthesis of two-dimensional Fe, N-codoped graphene bifunctional oxygen electrocatalyst for rechargeable air-cathode, *Chem. Eng. J.* 411 (2021) 128492, <https://doi.org/10.1016/j.cej.2021.128492>.
- [54] Y. Gao, J. Zhu, H. An, P. Yan, B. Huang, R. Chen, F. Fan, C. Li, Directly probing charge separation at interface of TiO_2 phase junction, *J. Phys. Chem. C* 8 (2017) 1419–1423, <https://doi.org/10.1021/acs.jpcclett.7b00285>.
- [55] Y.X. Lin, S.N. Zhang, Z.H. Xue, J.J. Zhang, H. Su, T.J. Zhao, G.Y. Zhai, X.H. Li, M. Antonietti, J.S. Chen, Boosting selective nitrogen reduction to ammonia on electron-deficient copper nanoparticles, *Nat. Commun.* 10 (2019) 4380, <https://doi.org/10.1038/s41467-019-12312-4>.
- [56] D. Zhao, K. Sun, W.C. Cheong, L. Zheng, C. Zhang, S. Liu, X. Cao, K. Wu, Y. Pan, Z. Zhuang, B. Hu, D. Wang, Q. Peng, C. Chen, Y. Li, Synergistically interactive pyridinic-N-MoP sites: identified active centers for enhanced hydrogen evolution in alkaline solution, *Angew. Chem. Int. Ed.* 59 (2019) 8982–8990, <https://doi.org/10.1002/anie.201908760>.
- [57] Y.-C. Hao, Y. Guo, L.-W. Chen, M. Shu, X.-Y. Wang, T.-A. Bu, W.-Y. Gao, N. Zhang, X. Su, X. Feng, J.-W. Zhou, B. Wang, C.-W. Hu, A.-X. Yin, R. Si, Y.-W. Zhang, C.-H. Yan, Promoting nitrogen electroreduction to ammonia with bismuth nanocrystals and potassium cations in water, *Nat. Catal.* 2 (2019) 448–456, <https://doi.org/10.1038/s41929-019-0241-7>.
- [58] Q. Dang, S. Tang, T. Liu, X. Li, X. Wang, W. Zhong, Y. Luo, J. Jiang, Regulating electronic spin moments of single-atom catalyst sites via single-atom promoter tuning on S-vacancy MoS_2 for efficient nitrogen fixation, *J. Phys. Chem. Lett.* 12 (2021) 8355–8362, <https://doi.org/10.1021/acs.jpcclett.1c02432>.
- [59] M. Li, H. Zhu, Q. Yuan, T. Li, M. Wang, P. Zhang, Y. Zhao, D. Qin, W. Guo, B. Liu, X. Yang, Y. Liu, Y. Pan, Proximity electronic effect of Ni/Co diatomic sites for synergistic promotion of electrocatalytic oxygen reduction and hydrogen evolution, *Adv. Funct. Mater.* 33 (2022) 2210867, <https://doi.org/10.1002/adfm.202210867>.
- [60] Y. Gu, B. Xi, W. Tian, H. Zhang, Q. Fu, S.L. Xiong, Boosting elective nitrogen reduction via geometric coordination engineering on single-tungsten-atom catalysts, *Adv. Mater.* 33 (2021) 2100429, <https://doi.org/10.1002/adma.202100429>.